Three-Dimensional Lattice Boltzmann Simulation of Two-Phase Flow Containing a Deformable Body with a Viscoelastic Membrane

Toshiro Murayama[1,2], Masato Yoshino[3,4,*] and Tetsuo Hirata[3]

[1] *Department of Mathematics and System Development Engineering, Interdisciplinary Graduate School of Science and Technology, Shinshu University, 4-17-1, Wakasato, Nagano-shi, Nagano 380-8553, Japan*
[2] *Satellite Venture Business Laboratory (SVBL), Shinshu University, 3-15-1, Tokida, Ueda-shi, Nagano 386-8567, Japan*
[3] *Department of Mechanical Systems Engineering, Faculty of Engineering, Shinshu University, 4-17-1, Wakasato, Nagano-shi, Nagano 380-8553, Japan*
[4] *CREST, Japan Science and Technology Agency, 4-1-8, Honcho, Kawaguchi-shi, Saitama 332-0012, Japan*

Abstract. The lattice Boltzmann method (LBM) with an elastic model is applied to the simulation of two-phase flows containing a deformable body with a viscoelastic membrane. The numerical method is based on the LBM for incompressible two-phase fluid flows with the same density. The body has an internal fluid covered by a viscoelastic membrane of a finite thickness. An elastic model is introduced to the LBM in order to determine the elastic forces acting on the viscoelastic membrane of the body. In the present method, we take account of changes in surface area of the membrane and in total volume of the body as well as shear deformation of the membrane. By using this method, we calculate two problems, the behavior of an initially spherical body under shear flow and the motion of a body with initially spherical or biconcave discoidal shape in square pipe flow. Calculated deformations of the body (the Taylor shape parameter) for various shear rates are in good agreement with other numerical results. Moreover, tank-treading motion, which is a characteristic motion of viscoelastic bodies in shear flows, is simulated by the present method.

AMS subject classifications: 74F10, 76M28, 74L15

Key words: lattice Boltzmann method (LBM), two-phase flow, viscoelastic membrane, shear flow, tank-treading motion.

*Corresponding author. *Email addresses:* s08t206@shinshu-u.ac.jp (T. Murayama), masato@shinshu-u.ac.jp (M. Yoshino), hirata@shinshu-u.ac.jp (T. Hirata)

1 Introduction

Problems of solid–fluid two-phase flow containing deformable bodies can be found, for example, in biological fields connected with blood flow in capillaries. In this problem, the interaction between red blood cells (RBCs) and blood plasma becomes important in small blood vessels where the cellular size is comparable to the vessel diameter. A normal RBC is easily deformed, and the deformability of the RBC is related to the erythrocyte configuration, the viscosity of the internal fluid, and the viscoelasticity of the membrane [1, 2]. In particular, the elastic behavior of the RBC is determined by the nature of the elastic membrane. Although investigations of the complicated behavior of the RBC are needed, it is difficult to examine the phenomena that are involved, particularly in microscale vessels, by means of experiments. Therefore, numerical simulation is considered to be an effective approach for microscopic investigation of such flow problems.

With regard to numerical studies of solid–fluid two-phase flows, Ramanujan and Pozrikidis [3] studied the deformation of a liquid capsule enclosed by an elastic membrane in shear flows with the boundary element method. Boryczko et al. [4] and Dzwinel et al. [5] have proposed discrete particle models for simulation of RBCs in capillary vessels by the Lagrangian coordinates technique. Tsubota et al. [6] carried out a simulation based on the particle method [7] to examine a peculiar rotary motion (i.e., tank-treading motion [8, 9]). Although these studies have produced interesting results, because of the complexity of the algorithms employed for the solid–fluid coupling problems, elaborate computing code is required and computation times are rather long.

Recently, the lattice Boltzmann method (LBM) [10–12] has been developed into an alternative and promising numerical scheme for simulating multicomponent and multiphase fluid flows. In particular, for solid–fluid two-phase flows, Ladd [13–15] was the first to simulate solid–fluid suspensions of spheres in shear flows. In addition, flow problems including deformable bodies are simulated by combining LBM with various methods. Sui et al. [16, 17] simulated the motion of a body with elastic membrane in shear flows by using an immersed boundary method. Dupin et al. [18, 19] also simulated the motion of red blood cells in fluid flows. They discretized the 3D capsule membrane into flat triangular elements, and the elastic forces acting at the triangle vertices are inserted in LBM nodes. The authors [20] have recently investigated behavior of a deformable body with viscoelastic membranes in two-dimensional flows. In the present study, we extend the numerical method to three-dimensions, and moreover, we take account of changes in surface area of the membrane and in total volume of the body as well as shear deformation of the membrane. By using the method, we simulate the behavior of a viscoelastic body under shear flow and the motion of a viscoelastic body in square pipe flow.

The paper is organized as follows. In Section 2, we describe how to determine the elastic forces acting on the viscoelastic membrane of the body and how to introduce elastic force into the two-phase LBM. In Section 3, we present numerical results of the behavior of a deformable body in two flow fields: under shear flow and in square pipe flow. Finally, concluding remarks are given in Section 4.

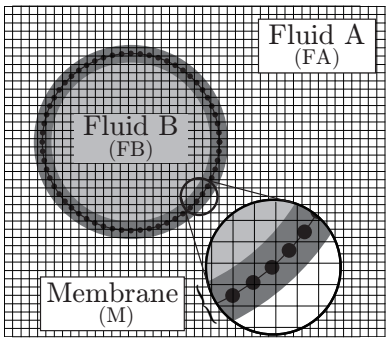

Figure 1: Model of a body with viscoelastic membrane.

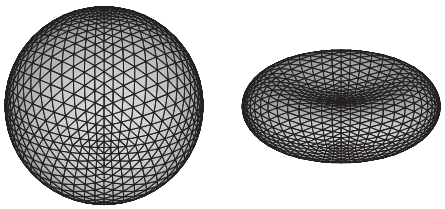

Figure 2: Discretization of body with spherical shape (left) and biconcave discoidal shape (right).

Figure 3: Diagram of triangular mesh (left) and spring model (right).

2 Numerical method

As described in [21], we use nondimensional variables defined by a characteristic length L, a characteristic particle speed c, a characteristic time scale $t_0 = L/U$ where U is a characteristic flow speed, a reference order parameter ϕ_0, and a reference density ρ_0. The three-dimensional 15-velocity model is used in the present study. The velocity vectors of this model are given by $\boldsymbol{c}_i = (0, 0, 0)$, $(\pm 1, 0, 0)$, $(0, \pm 1, 0)$, $(0, 0, \pm 1)$, $(\pm 1, \pm 1, \pm 1)$.

2.1 Model of body with viscoelastic membrane

Because the viscous effect of the body is inherent in the original LBM for two-phase flows, only an elastic force based on the Kelvin–Voigt model needs to be introduced into the LBM. As shown in Fig. 1, a body with a viscoelastic membrane of a finite but relatively thin thickness is considered, where the membrane is composed of particles that are connected with their neighboring particles by springs. The body has an internal viscous fluid covered by the viscoelastic membrane. The internal fluid is referred to as Fluid B, which is distinguished from the surrounding viscous fluid called Fluid A. Because these fluids have their own character, it is required to distinguish them in some way to give different values of physical properties (e.g., viscosity). In the present model, these fluids are distinguished by an order parameter in the LBM for two-phase flows [22, 23] described later. However, the membrane is not autonomously determined but the region of the cubic lattices containing particles are assumed to be a membrane, so that the elastic force is

applied to all vertices of the cubic lattices. An elastic model based on the minimum energy principle [6] is introduced to the LBM in order to determine the elastic force acting on the viscoelastic membrane of the body.

Three-dimensional structural membrane models are discretized into flat triangular elements. The triangulation procedure is similar to those of Ramanujan and Pozrikidis [3] and of Sui et al. [16]. To discretize the unstressed interface, each triangular face of a regular octahedron is subdivided into 4^n triangular elements, where n is a positive integer. These elements are then projected radially onto a sphere. The geometry of each element is described by its three vertices. The discretization of a spherical surface is shown in Fig. 2 (left). The biconcave discoidal model in Fig. 2 (right) is constructed by means of the mapping system [24]. The parameters are the same as those by Sui et al. [16]. As shown in Fig. 3, the elastic membrane models are composed of small triangular elements connected by springs where Lagrangian particles are positioned at the vertices. A body with a viscoelastic membrane which encloses a viscous fluid has mechanical property of elastic resistances to the stretching, dilation, and bending. For example, a normal RBC and a vesicle have strong resistance to the dilation of the body as well as to the stretching of the membrane. This is attributed to the fact that such bodies have an inherent property of conserving surface area of the membrane and total volume of the body. Moreover, in the case of a body with a thin viscoelastic membrane, the effect of the elastic resistance to the bending is negligibly smaller than that of the others [25]. Therefore, only the resistances to the stretching and dilation are introduced in the present model.

First, the elastic resistance to the stretching of the membrane is described. We assume that this resistance force is modeled by the stretching force of the spring. The membrane is composed of the N particles P_j(j=1, 2, 3, …, N). Moreover, the particles are connected by M elastic springs that have an initial length $l_{m0}(m = 1,\ 2,\ 3,\ \ldots,\ M)$ and an elastic modulus K^{l}_m. The elastic energy E^{l} stored in the stretch/compression of the spring due to change in the length l_m from its reference l_{m0} is expressed as

$$E^{\mathrm{l}} = \frac{1}{2}\sum_{m=1}^{M} K^{\mathrm{l}}_m \left(\frac{l_m - l_{m0}}{l_{m0}}\right)^2, \tag{2.1}$$

where l_m is the stretch/compression displacement between the two particles P_j and P_k at the positions $\boldsymbol{r}_j$ and $\boldsymbol{r}_k$.

Next, the elastic resistance to the dilation of the body is described. We assume that there are two contributions to this elastic resistance: (i) surface area of the membrane; (ii) total volume of the body. Hence, in the present model, we take account of the elastic forces based on the resistance to changes in area of triangular elements and in total surface area of the membrane. As shown in Fig. 3, we define the following quantities and notations: e is the index of a triangular element consisting of a membrane, A_e is the area of the element e, and A is the total surface area of the membrane. The energy E^{A}

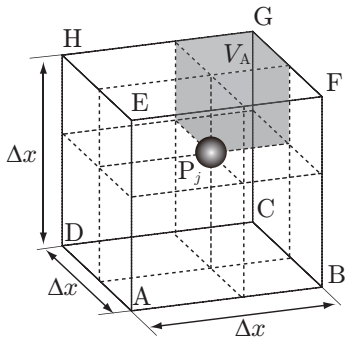

Figure 4: Cubic lattice with sides Δx where particle P_j is included. The weighting coefficient $\omega(A)$ is equal to the shaded volume V_A divided by volume $(\Delta x)^3$ of the cubic lattice.

generated by change in the surface area of the membrane is given by

$$E^{A} = \frac{1}{2}K^{a}\sum_{e=1}^{N_e}\left(\frac{A_e - A_{e0}}{A_{e0}}\right)^2 + \frac{1}{2}K^{A}\left(\frac{A - A_0}{A_0}\right)^2, \tag{2.2}$$

where K^{a} and K^{A} are the elastic moduli for dilation of the local area and total surface area, respectively, the subscript 0 indicates the initial value, and N_e is the number of elements. In addition, the energy E^{V} generated by change in the total volume of the body (from initial value V_0 to V) is expressed as

$$E^{V} = \frac{1}{2}K^{V}\left(\frac{V - V_0}{V_0}\right)^2, \tag{2.3}$$

where K^{V} is the elastic modulus for dilation of the total volume. On the basis of the energy principle, the behavior of the body is determined by moving the particles so that the total elastic energy $E = E^{l} + E^{A} + E^{V}$ leads to a minimum value. According to the principle of virtual work, the elastic force acting on the particle is determined as

$$\boldsymbol{F}_j = -\frac{\partial E}{\partial \boldsymbol{r}_j}. \tag{2.4}$$

2.2 Coupling of particle and fluid dynamics

The dynamic behavior of the particles is as follows. Let $\boldsymbol{r}_j$ be the position of a particle P_j and $\boldsymbol{x}_\Psi$ the position of a fluid lattice node Ψ in Cartesian coordinates. During the time-step Δt, the particle P_j at the position $\boldsymbol{r}_j(t)$ moves to the position given by the following equation:

$$\boldsymbol{r}_j(t + \Delta t) = \boldsymbol{r}_j(t) + \boldsymbol{u}_j(t)\Delta t, \tag{2.5}$$

where $\boldsymbol{u}_j(t)$ is the velocity of the particle. As shown in Fig. 4, the velocity $\boldsymbol{u}_j(t)$ is obtained by the linear interpolation of the fluid velocities $\boldsymbol{u}(\boldsymbol{x}_\Psi,t)$ at the surrounding eight nodes, $\Psi=$A, B, C, …, and H, which indicate the vertices of the cubic lattice with sides Δx where the particle P_j is included:

$$\boldsymbol{u}_j(t)=\sum_{\Psi}\omega(\Psi)\boldsymbol{u}(\boldsymbol{x}_\Psi,t) \quad \text{for } \Psi=\text{A, B, C, …, H,} \tag{2.6}$$

where $\omega(\Psi)$ is the weighting coefficient such that $\sum_\Psi\omega(\Psi)=1$. The weighting coefficient $\omega(\Psi)$ is related to the diagonally opposite, cuboidal volume defined by the position of the particle; e.g., for $\Psi=$A in Fig. 4, the weighting coefficient $\omega(\mathrm{A})$ is equal to the shaded volume V_A divided by the volume $(\Delta x)^3$ of the cubic lattice. At the same time, the displacement of the springs, surface area, and total volume are changed, and the particle is subject to an elastic force $\boldsymbol{F}_j$, as given by Eq. (2.4). In addition, because the particle does not lie on lattice nodes, the redistribution of the elastic force at P_j to the surrounding lattice nodes is carried out by the linear extrapolation. Similarly, the elastic force acting on the particle P_j multiplied by the weighting coefficient is distributed to the eight lattice nodes of the cube containing the particle. The elastic force $\boldsymbol{F}_j(\boldsymbol{x}_\Psi,t)$ at the lattice node Ψ distributed from the particle P_j is given by

$$\boldsymbol{F}_j(\boldsymbol{x}_\Psi,t)=\omega(\Psi)\boldsymbol{F}_j(t). \tag{2.7}$$

The net elastic force $\boldsymbol{F}(\boldsymbol{x}_\Psi,t)$ at the lattice node Ψ can be obtained by sum of the contributions from the relevant particles. Hence, $\boldsymbol{F}(\boldsymbol{x}_\Psi,t)$ is given by

$$\boldsymbol{F}(\boldsymbol{x}_\Psi,t)=\sum_{j=1}^{N}\boldsymbol{F}_j(\boldsymbol{x}_\Psi,t)\delta(\boldsymbol{r}_j,\boldsymbol{x}_\Psi), \tag{2.8}$$

where $\delta(\boldsymbol{r}_j,\boldsymbol{x}_\Psi)$ is the function to cut off nodes that are too distant from $\boldsymbol{r}_j$ to be included in the calculation [18, 19]. In the three-dimensional model, we need to consider particles in a reference domain around the lattice node Ψ, which is composed of eight cubes where Ψ is a vertex. Thus, $\delta(\boldsymbol{r}_j,\boldsymbol{x}_\Psi)$ is given by

$$\delta(\boldsymbol{r}_j,\boldsymbol{x}_\Psi)=\begin{cases}1 & \text{if the particle } \mathrm{P}_j \text{ is in the reference domain,}\\ 0 & \text{otherwise.}\end{cases} \tag{2.9}$$

2.3 Formulation in LBM

The numerical algorithm of fluid flows is based mainly on the LBM for incompressible two-phase fluid flows with the same density proposed by Inamuro et al. [22, 23]. In the calculations, the physical domain is divided into a cubic lattice, and the evolution of particle population at each lattice node is computed.

Two particle velocity distribution functions, f_i and g_i, are used. The function f_i is used for the calculation of an order parameter which represents two phases, and the function

g_i is used for the calculation of the pressure and the velocity of the two-phase fluids with the same density. The evolution of the particle distribution functions $f_i(\boldsymbol{x},t)$ and $g_i(\boldsymbol{x},t)$ with velocity $\boldsymbol{c}_i$ at the lattice node $\boldsymbol{x}$ and at time t is computed by

$$f_i(\boldsymbol{x}+\boldsymbol{c}_i\Delta x,t+\Delta t)=f_i^c(\boldsymbol{x},t), \tag{2.10}$$
$$g_i(\boldsymbol{x}+\boldsymbol{c}_i\Delta x,t+\Delta t)=g_i^c(\boldsymbol{x},t), \tag{2.11}$$

where f_i^c and g_i^c are functions of macroscopic variables and their derivatives given below, and Δt is a time-step during which the particles travel the lattice spacing Δx. It should be noted that the present method is based on the lattice kinetic scheme [21] which is an improved scheme of the LBM.

The order parameter ϕ distinguishing the two phases and the macroscopic variables of two-phase fluids (the pressure p and the velocity $\boldsymbol{u}$) are defined in terms of the two particle velocity distribution functions:

$$\phi = \sum_{i=1}^{15} f_i, \tag{2.12}$$
$$p = \frac{1}{3}\sum_{i=1}^{15} g_i, \tag{2.13}$$
$$\boldsymbol{u} = \sum_{i=1}^{15} g_i \boldsymbol{c}_i. \tag{2.14}$$

The function f_i^c in Eq. (2.10) is given by

$$f_i^c = H_i\phi + F_i\left(p_0-\kappa_f\phi\nabla^2\phi-\frac{\kappa_f}{6}|\nabla\phi|^2\right)+3E_i\phi c_{i\alpha}u_\alpha+E_i\kappa_f G_{\alpha\beta}c_{i\alpha}c_{i\beta}, \tag{2.15}$$

with

$$p_0=\phi T\frac{1}{1-b\phi}-a\phi^2, \tag{2.16}$$

and

$$G_{\alpha\beta}=\frac{9}{2}\frac{\partial\phi}{\partial x_\alpha}\frac{\partial\phi}{\partial x_\beta}-\frac{3}{2}\frac{\partial\phi}{\partial x_\gamma}\frac{\partial\phi}{\partial x_\gamma}\delta_{\alpha\beta}, \tag{2.17}$$

where $\alpha,\beta,\gamma=x,y,z$ (subscripts α, β, and γ represent Cartesian coordinates and the summation convention is used), κ_f is a constant parameter determining the width of the interface, a, b, and T are free parameters determining the maximum and minimum values of ϕ, $\delta_{\alpha\beta}$ is the Kronecker delta, and the coefficients are

$$\left.\begin{aligned}
&E_1=2/9, E_2=E_3=E_4=\cdots=E_7=1/9,\\
&E_8=E_9=E_{10}=\cdots=E_{15}=1/72,\\
&H_1=1, H_2=H_3=H_4=\cdots=H_{15}=0,\\
&F_1=-7/3, F_i=3E_i\,(i=2,3,4,\ldots,15),
\end{aligned}\right\}. \tag{2.18}$$

Note that Eq. (2.16) is the Van der Waals equation of state, which is one choice among several types of equation of state. On the other hand, the function g_i^c in Eq. (2.11) is given with an additional term related to the elastic force as follows:

$$\begin{aligned} g_i^c &= E_i\left[3p+3c_{i\alpha}u_\alpha-\frac{3}{2}u_\alpha u_\alpha+\frac{9}{2}c_{i\alpha}c_{i\beta}u_\alpha u_\beta+\frac{3}{4}\Delta x\left(\frac{\partial u_\beta}{\partial x_\alpha}+\frac{\partial u_\alpha}{\partial x_\beta}\right)c_{i\alpha}c_{i\beta}\right] \\ &\quad +3E_i c_{i\alpha}\frac{\partial}{\partial x_\beta}\left[\mu\left(\frac{\partial u_\beta}{\partial x_\alpha}+\frac{\partial u_\alpha}{\partial x_\beta}\right)\right]\Delta x+3E_i\delta_{\Pi\mathrm{M}}F_\alpha c_{i\alpha}, \end{aligned} \tag{2.19}$$

where $\Pi = \mathrm{FA},\mathrm{FB},\mathrm{M}$ (subscripts FA, FB, and M indicate fluid phase A, fluid phase B, and membrane, respectively), μ is the viscosity, F_α is the elastic force described in Section 2.2, and $\delta_{\Pi\mathrm{M}}$ is the Kronecker delta. It should be noted that the interfacial tension is assumed to be free in the present study in order to investigate only the effect of the elastic force. The last term $3E_i\delta_{\Pi\mathrm{M}}F_\alpha c_{i\alpha}$ in the right-hand side of Eq. (2.19) is an external force term to recover an elastic force $\boldsymbol{F}$ acting on the membrane in the macroscopic level. For the calculation of the first and second derivatives in Eqs. (2.15), (2.17), and (2.19), the following finite-difference approximations given by the Taylor series expansion are used:

$$\frac{\partial\psi}{\partial x_\alpha} \approx \frac{1}{10\Delta x}\sum_{i=2}^{15}c_{i\alpha}\psi(\boldsymbol{x}+\boldsymbol{c}_i\Delta x), \tag{2.20}$$

$$\nabla^2\psi \approx \frac{1}{5(\Delta x)^2}\left[\sum_{i=2}^{15}\psi(\boldsymbol{x}+\boldsymbol{c}_i\Delta x)-14\psi(\boldsymbol{x})\right]. \tag{2.21}$$

As in [21, 22], applying the asymptotic theory [26, 27] to Eqs. (2.10)–(2.19), we can obtain the phase-field advection–diffusion equation (the Cahn–Hilliard equation plus advection), the continuity equation, and the Navier–Stokes equations including the elastic force as an external force term for incompressible fluids with relative errors of $\mathrm{O}[(\Delta x)^2]$. As mentioned in Section 2.1, the surrounding fluid (Fluid A) and the internal fluid (Fluid B) are not generally the same. In the present study, however, these two fluids are assumed to be the same Newtonian fluid without elasticity in order to compare the present results with those by the available previous work [16]. Thus, the viscosities of the surrounding and the internal fluids are specified as the same value in the following simulations.

2.4 Algorithm of computation

We now summarize the algorithm of computation.

Step 1. Compute $\boldsymbol{u}_j(t)$ using Eq. (2.6), and then compute $\boldsymbol{r}_j(t+\Delta t)$ using Eq. (2.5) with the obtained $\boldsymbol{u}_j(t)$.

Step 2. Using Eqs. (2.10) and (2.11), compute $f_i(\boldsymbol{x},t+\Delta t)$ and $g_i(\boldsymbol{x},t+\Delta t)$, and then compute $\phi(\boldsymbol{x},t+\Delta t)$, $p(\boldsymbol{x},t+\Delta t)$, and $\boldsymbol{u}(\boldsymbol{x},t+\Delta t)$ with Eqs. (2.12)–(2.14).

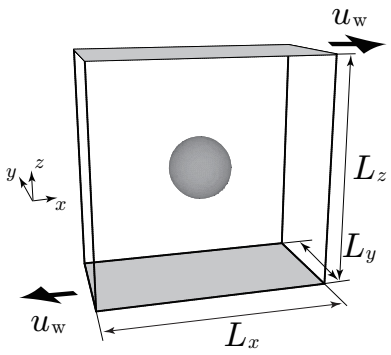

Figure 5: Computational domain of deformation of body under shear flow. The body is represented by the iso-surface of the order parameter $\phi = (\phi_{\max} + \phi_{\min})/2$.

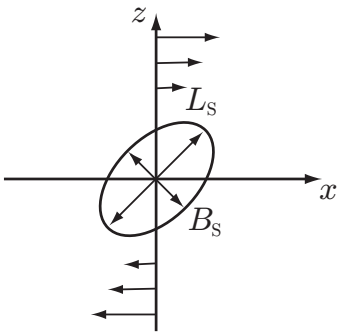

Figure 6: Body deformation under shear flow: B_S, minor axis; L_S, length perpendicular to the minor axis.

Step 3. Using Eqs. (2.1)–(2.4), compute $\boldsymbol{F}_j(t+\Delta t)$, and then compute $\boldsymbol{F}(\boldsymbol{x},t+\Delta t)$ with Eqs. (2.7)–(2.9).

Step 4. Advance one time step and return to Step 1.

3 Results and discussion

3.1 Deformation of a body under shear flow

The transient deformation of a spherical body with a viscoelastic membrane under shear flow is investigated. As shown in Fig. 5, a viscoelastic body with radius R is placed at the center in a suspending fluid between two parallel walls with length L_z apart. The size of the whole domain is $L_x \times L_y \times L_z = 120\Delta x \times 60\Delta x \times 120\Delta x$. The membrane is composed of N particles ($N = 258$), and the thickness of the membrane is approximately $2\Delta x$. The initial distance between the centroid and each particle is set to be $R = 12\Delta x$. The body is brought to the equilibrium state at rest and at $t = 0$, the top and bottom walls begin to move with velocities u_w and $-u_w$, respectively. The no-slip boundary condition is used on the moving walls, and the periodic boundary condition is used on the other sides of the domain.

It is noted that the dimensionless parameters for this problem are the Reynolds number ($\mathrm{Re} = \rho_{FA}\Gamma R^2/\mu_{FA}$), the dimensionless shear rate ($G = \mu_{FA}\Gamma R/K^1$), and the ratio of the viscosity of the internal fluid to that of the surrounding fluid ($\eta = \mu_{FB}/\mu_{FA}$), where $\Gamma = 2u_w/L_z$ is the shear rate [16], μ_{FA} and μ_{FB} are the viscosities of Fluids A and B, respectively, and $K^1 = K^1_m/l^2_{m0}$ is elastic modulus for shear strain of the membrane. The parameter η is kept at unity because Fluids A and B are assumed to be identical in the present simulations. In addition, the ratios of the elastic moduli based on local area, total surface

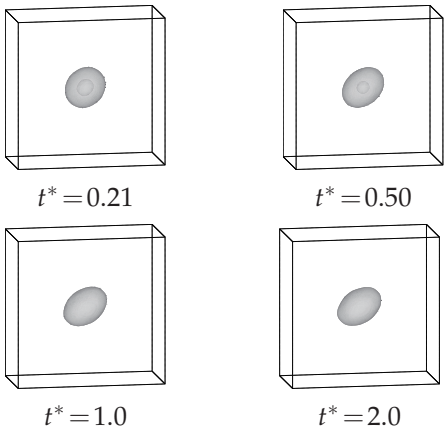

Figure 7: Temporal evolution of body shape for $G=0.075$ at $\mathrm{Re}=0.025$. The body is represented by the iso-surface of the order parameter $\phi=(\phi_{\max}+\phi_{\min})/2$. $t^*=t\Gamma$ is the dimensionless time.

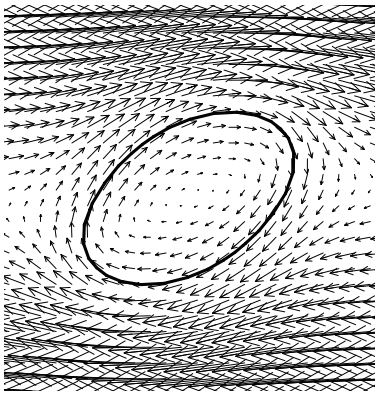

Figure 8: Close-up of velocity vectors around deformed body in steady state on $y/L_y=0.50$ for $G=0.075$ at $\mathrm{Re}=0.025$. The bold line represents the membrane.

area, and total volume of the body to that for shear strain ($C^{\mathrm{a}}=K^{\mathrm{a}}/\overline{K_m^{\mathrm{l}}}$, $C^{\mathrm{A}}=K^{\mathrm{A}}/\overline{K_m^{\mathrm{l}}}$, and $C^{\mathrm{V}}=K^{\mathrm{V}}/\overline{K_m^{\mathrm{l}}}$), where $\overline{K_m^{\mathrm{l}}}$ is the space-averaged value of the elastic modulus of springs for shear strain, are also important parameters. However, the elastic moduli are given as $K^{\mathrm{a}}=K^{\mathrm{A}}=K^{\mathrm{V}}=\overline{K_m^{\mathrm{l}}}$ for comparison with other numerical results, so that the parameters become $C^{\mathrm{a}}=C^{\mathrm{A}}=C^{\mathrm{V}}=1$. We chose $a=9/49$, $b=2/21$, and $T=0.55$ in Eq. (2.16); it follows that the maximum and minimum values of the order parameter are $\phi_{\max}=4.937$ and $\phi_{\min}=2.251$. The parameter κ_f is fixed at $0.01(\Delta x)^2$. The body deformation is defined by the Taylor shape parameter $D_{xz}=(L_{\mathrm{S}}-B_{\mathrm{S}})/(L_{\mathrm{S}}+B_{\mathrm{S}})$, where L_{S} and B_{S} are the major and minor axes of the body, respectively (see Fig. 6). Note that the larger the body deformation is, the more D_{xz} increases.

First, the deformation of the spherical body with the dimensionless shear rate G ranging from 0.0375 to 0.3 is investigated. The Reynolds number is fixed at 0.025. The time evolutions of the body shape for $G=0.075$ are shown in Fig. 7, where the dimensionless time is defined by $t^*=t\Gamma$. Note that the body is represented by the iso-surface of the order parameter $\phi=(\phi_{\max}+\phi_{\min})/2$, and that the depiction of the body shape in the following figures is the same as that in Fig. 7. It is found that the body is stretched out and becomes deformed into an elongated ellipsoidal shape with inclination as time passes. Also, the deformation of the body finally becomes time-independent. Close-up of velocity vectors around the body in the steady state on $y/L_y=0.50$ is presented in Fig. 8. From this figure, a rotating flow inside the body and a circulating flow around the body are observed. These flow characteristics are similar to those found by Zahalak et al. [28].

Next, the temporal evolutions of the Taylor shape parameter D_{xz} are shown in Fig. 9. In this figure, the results of Sui et al. [16] by means of the immersed boundary method are also shown. Both results are found to be in good agreement with each other. Also, for various parameters G, the shapes of the body in the steady state on $y/L_y=0.50$ are

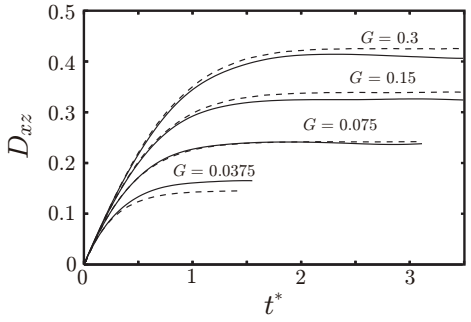

Figure 9: Temporal evolution of Taylor shape parameter D_{xz} ($t^* = t\Gamma$). The dashed line represents results by Sui et al. [16].

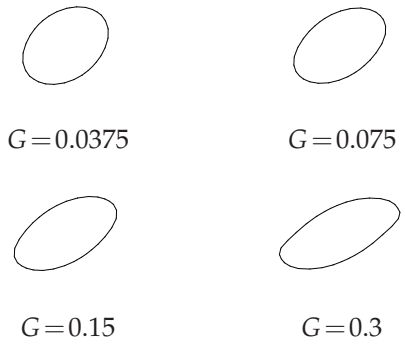

Figure 10: Body shape in the steady state on $y/L_y = 0.50$ under shear flow.

presented in Fig. 10. It is seen that for low G, the body slightly deforms and the shapes are ellipsoidal, but for high G, they become slender and sigmoidal owing to its large deformation. These shapes are similarly observed for a viscous liquid drop under simple shear flows, in which the effect of the interfacial tension is considered [22, 29, 30]. In the case of a liquid drop, however, the drop continues to deform and eventually breaks up as the shear rate becomes larger, whereas the body evolves to a steady shape without disintegration. Moreover, the rate of deformation of the body is large for low G, and it monotonically diminishes with increasing G. This tendency is also seen in other numerical studies [3,16]. In addition, we examine the variations in surface area of the membrane and in total volume of the body during the deformation. Note that the total volume decreases and the surface area increases since the initial state. It is found that the relative change of the surface area is rather large (8.9% in the case of $G = 0.3$), though the relative change of the total volume is small (2.1% at most). This result indicates that these variations (especially the variation in the surface area of the membrane) are directly linked to the deformation of the body.

In addition, the motion of the membrane is investigated. Figs. 11 and 12 show the unsteady behavior of the membrane and the temporal position of a certain particle, respectively for $G = 0.075$ at $\mathrm{Re} = 0.25$. From these figures, it is found that the membrane performs an ellipsoidal rotation with a constant period ($\approx 17t^*$). This periodic motion is generally called the tank-treading motion [8, 9], which is a rotary motion like that of a caterpillar track. Thus, an interesting phenomenon characteristic of RBC behavior can be simulated by the present method. In the case of the largest deformation (for $G = 0.3$), the relative error between initial mass and final mass of the fluid phase (the region occupied by Fluids A and B) is less than 0.35%. Hence, the mass conservation for each phase is verified in the present simulations. We also calculate the behavior of the body with initially an non-spherical shape, namely, a biconcave discoidal shape. The tank-treading motion is observed for the body with high deformability. For a body with low deformability, on

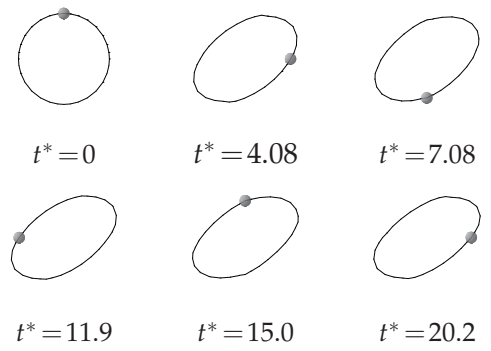

Figure 11: Unsteady rotary motion of membrane for $G=0.075$ at $\mathrm{Re}=0.25$. The gray circle indicates a certain particle in the membrane ($t^*=t\Gamma$).

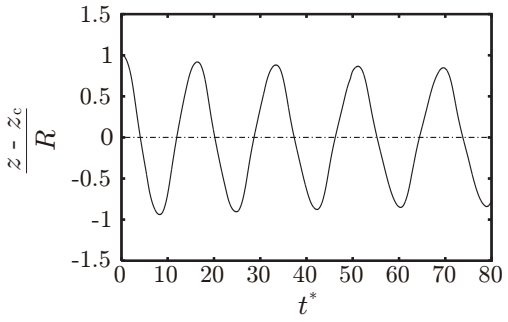

Figure 12: Temporal position of a certain particle in the membrane for $G=0.075$ at $\mathrm{Re}=0.25$. z_c is the z-position of the centroid of the body ($t^*=t\Gamma$).

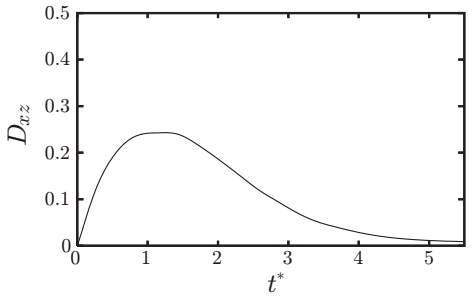

Figure 13: Temporal evolution of Taylor shape parameter D_{xz} for $G=0.075$ at $\mathrm{Re}=0.25$ ($t^*=t\Gamma$).

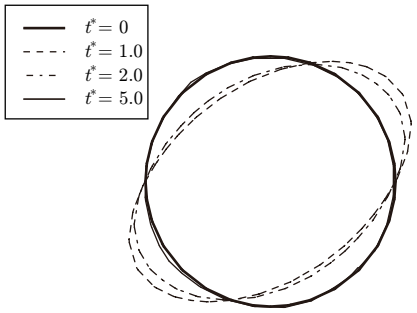

Figure 14: Snapshots of body shape on $y/L_y=0.50$ under shear flow for $G=0.075$ at $\mathrm{Re}=0.25$ ($t^*=t\Gamma$).

the other hand, we observe the tumbling motion [31, 32], which is an unsteady flipping motion of the whole body as well as the viscoelastic membrane. However, as the elastic modulus becomes larger, numerical instability occurs for the present lattice resolution. One main reason for the instability would be complicated configuration of the membrane due to lack of bending resistance.

Finally, the restoration of the deformed body for $G=0.075$ at $\mathrm{Re}=0.25$ is investigated. At $t^*=0$, the top and bottom walls begin to move with velocities u_w and $-u_\mathrm{w}$, respectively. At $t^*=1.0$, we cease the movement of the walls so as to examine the restoration of the deformed body. The temporal evolutions of the Taylor shape parameter D_{xz} are shown in Fig. 13. In addition, snapshots of the body shape on $y/L_y=0.50$ at various times are presented in Fig. 14. From these figures, it is found that the body restores to its original state after the deformation. Thus, the present results indicate that the effectiveness of the viscoelastic membrane model is demonstrated.

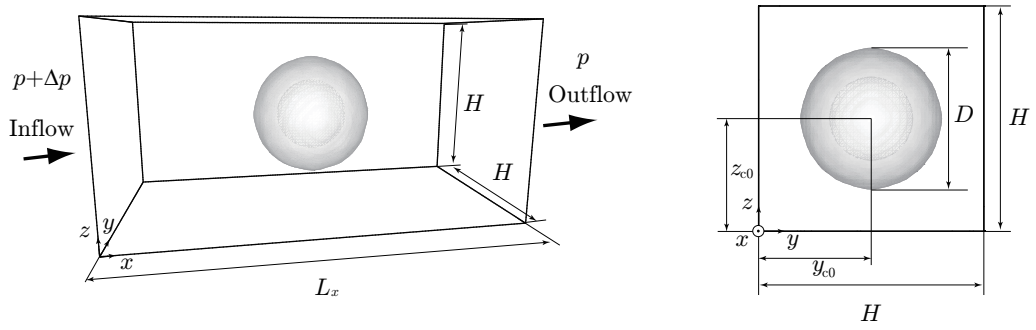

Figure 15: Computational domain (left) and cross section (right) of motion of body in square pipe flow. The body is represented by the iso-surface of the order parameter $\phi = (\phi_{\max} + \phi_{\min})/2$.

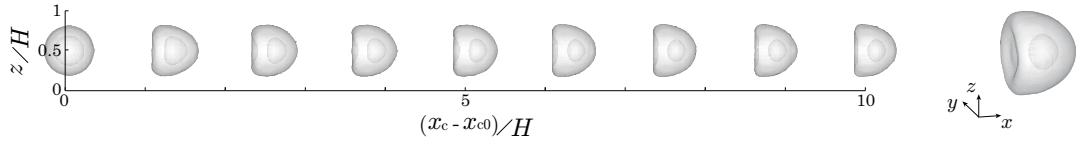

Figure 16: Time variations of shape and position of body (left) and snapshots of the body in the steady state (right) for $K^{\mathrm{l}} = 1.5 \times 10^{-5} \Delta x$ at $\mathrm{Re} = 0.71$. The body is represented by the iso-surface of the order parameter $\phi = (\phi_{\max} + \phi_{\min})/2$. The initial shape of the body is a sphere.

3.2 Motion of a body in square pipe flow

The motion of a body with a viscoelastic membrane in square pipe flow is investigated. As shown in Fig. 15, a rectangular domain having the square section with sides H is considered. The size of the whole domain is $L_x \times H \times H = 128\Delta x \times 64\Delta x \times 64\Delta x$. A body with diameter $D = 32\Delta x$ is placed at $(x_{\mathrm{c}0}/L_x,\ y_{\mathrm{c}0}/H,\ z_{\mathrm{c}0}/H) = (0.50,\ 0.50,\ 0.50)$, where $(x_{\mathrm{c}0},\ y_{\mathrm{c}0},\ z_{\mathrm{c}0})$ is the initial position of the centroid of the body. In this problem, the elastic modulus of shear strain is set to $K^{\mathrm{l}} = 1.5 \times 10^{-5} \Delta x$ for both a spherical body and a biconcave disk. Also, the other elastic moduli are set to $K^{\mathrm{a}} = 0.01\overline{K^{\mathrm{l}}_m}$ and $K^{\mathrm{A}} = K^{\mathrm{V}} = \overline{K^{\mathrm{l}}_m}$; it follows that $C^{\mathrm{a}} = 0.01$ and $C^{\mathrm{A}} = C^{\mathrm{V}} = 1$. The periodic boundary condition with a pressure difference is used at the inlet and outlet, and the no-slip boundary condition is used on the other boundaries. The gravitational effect is neglected; it follows that neutrally buoyant flow is assumed in the simulations. The parameters are the same as those in the previous problem. The Reynolds number, defined by $\mathrm{Re} = \rho_{\mathrm{FA}} H \overline{u}_{\mathrm{in}} / \mu_{\mathrm{FA}}$ where $\overline{u}_{\mathrm{in}}$ is the cross-sectional average of flow velocity at the inlet, is set to 0.71 in the simulations.

First, the deformation of a body with initially spherical shape is simulated. The shape and position of the body are shown in Fig. 16. It can be seen that the body becomes deformed into a concave shape on the upstream side and a convex shape on the downstream side like a parachute. We next simulate the deformation of a body whose initial shape is a biconcave disk. The shape and position of the body are shown in Fig. 17. From these results, it is seen that the body becomes deformed into shape like a parachute, re-

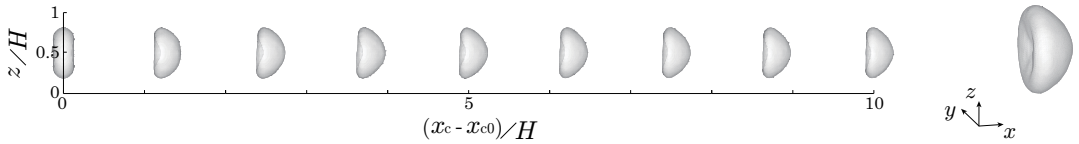

Figure 17: Time variations of shape and position of body (left) and snapshots of the body in the steady state (right) for $K^1 = 1.5 \times 10^{-5} \Delta x$ at $\mathrm{Re} = 0.71$. The body is represented by the iso-surface of the order parameter $\phi = (\phi_{\max} + \phi_{\min})/2$. The initial shape of the body is a biconcave disk.

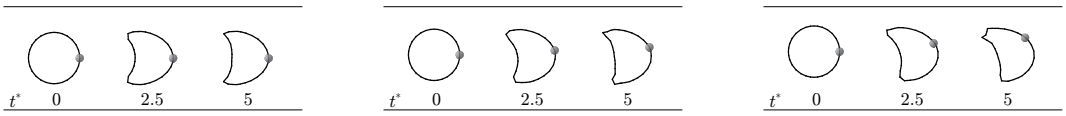

(a) $Z_0 = 0$ (b) $Z_0 = 0.063$ (c) $Z_0 = 0.13$

Figure 18: Time variations of shape and position of body for $K^1 = 1.5 \times 10^{-5} \Delta x$ at $\mathrm{Re} = 0.71$ ($t^* = t\overline{u}_{in}/D$).

gardless of whether the initial shape is a spherical body or a biconcave disk.

Next, in the case of the spherical body, the motion and deformation of the body which is initially released at various positions in the z-direction are shown in Fig. 18. The dimensionless time is defined by $t^* = t\overline{u}_{\mathrm{in}}/D$. The relative position Z_0 represents the initial distance between the centroid of the body and the center line of the pipe, $Z_0 = (z_{\mathrm{c0}} - H/2)/(H/2)$, and the positions in the x- and y-directions, x_{c0}/L_x and y_{c0}/H, are fixed at 0.50. It is seen that the body flows downstream with various shapes of deformation. The body which is released on the center line becomes deformed into shape like a parachute. On the other hand, the body whose initial position is off the center line becomes deformed into an asymmetric shape. Moreover, as the relative position Z_0 is larger, the shape on the wall side of the body becomes more elongated. This shape is usually called slipper shape [33]. In addition, a rotary motion of the body, i.e., the tank-treading motion can be seen in the cases of Fig. 18 (b) and (c). These results correspond to interesting phenomena frequently observed in capillaries such as small blood vessels [33].

Finally, the tip of the body can be seen in Fig. 18 (c), because the effect of the resistance to bending of the membrane is not taken into consideration in the present model. Although the bending modulus is smaller than the other moduli in the simulation of red blood cells [25], much longer computation without the bending resistance can cause wrinkles of the membrane [17]. Thus, the simulation including the effect of the bending resistance is required in future work.

4 Concluding remarks

The lattice Boltzmann method with an elastic model has been applied to the simulation of two-phase flows containing a deformable body with a viscoelastic membrane. By us-

ing the method, we investigated the behavior of the body under shear flow and in square pipe flow. Although the calculation of flow including several bodies and more quantitative investigations are required, the method can be a promising approach for simulating the complex behavior of viscoelastic bodies in capillaries, such as the motion of red blood cells in blood flows.

In this paper, the parameters concerning the elastic moduli are $C^{\mathrm{a}} = C^{\mathrm{A}} = C^{\mathrm{V}} = 1$ for the shear flow problem, and $C^{\mathrm{a}} = 0.01$ and $C^{\mathrm{A}} = C^{\mathrm{V}} = 1$ for the pipe flow problem. Besides, the viscosity ratio is fixed at $\eta = 1$ for both problems. However, their values are different from those for real human RBC membranes. For example, the ratio of the compressibility modulus to the elastic shear modulus, which is related to the above parameters concerning the elastic moduli, is measured to be 6.8×10^4 in the experiments by Waugh and Evans [34]. Also, the ratio of the viscosity of internal fluid in RBCs to that of plasma is normally $\eta = 5 \sim 6$. (According to the literatures [35, 36], for instance, the former is typically 6.0×10^{-3} Pa·s and the latter 1.2×10^{-3} Pa·s.) Therefore, the simulation for other values of the parameters is of importance in future work.

Acknowledgments

This research was supported in part by the Satellite Venture Business Laboratory, Shinshu University and by the Grant-in-Aid for Young Scientists (B) [No.21760123] of the Ministry of Education, Culture, Sports, Science and Technology, Japan. The authors also thank the anonymous referees for critical comments and helpful suggestions on the manuscript.

References

[1] T. Shiga, N. Maeda, and K. Kon, Erythrocyte rheology, Crit. Rev. Oncol. Hematol., 10 (1990), 9-48.

[2] N. Maeda and T. Shiga, Red cell aggregation, due to interactions with plasma proteins, J. Blood Rheol., 7 (1993), 3-12.

[3] S. Ramanujan and C. Pozrikidis, Deformation of liquid capsules enclosed by elastic membranes in simple shear flow: large deformations and the effect of fluid viscosities, J. Fluid Mech., 361 (1998), 117-143.

[4] K. Boryczko, W. Dzwinel, and D. A. Yuen, Dynamical clustering of red blood cells in capillary vessels, J. Mol. Model., 9 (2003), 16-33.

[5] W. Dzwinel, K. Boryczko, and D. A. Yuen, A discrete-particle model of blood dynamics in capillary vessels, J. Colloid Interface Sci., 258 (2003), 163-173.

[6] K. Tsubota, S. Wada, and T. Yamaguchi, Particle method for computer simulation of red blood cell motion in blood flow, Comput. Methods Programs Biomed., 83 (2006), 139-146.

[7] S. Koshizuka, H. Tamako, and Y. Oka, A particle method for incompressible viscous flow with fluid fragmentation, Comput. Fluid Dyn. J., 4 (1995), 29-46.

[8] T. M. Fischer and H. S. Schönbein, Tank treading motion of red cell membranes in viscometric flow: behavior of intracellular and extracellular markers (with film), Blood Cells, 3 (1977), 351-365.

[9] T. M. Fischer, On the energy dissipation in a tank-treading human red blood cell, Biophys. J., 32 (1980), 863-868.
[10] R. Benzi, S. Succi, and M. Vergassola, The lattice Boltzmann equation: theory and applications, Phys. Rep., 222 (1992), 145-197.
[11] S. Chen and G. D. Doolen, Lattice Boltzmann method for fluid flows, Annu. Rev. Fluid Mech., 30 (1998), 329-364.
[12] S. Succi, The Lattice Boltzmann Equation for Fluid Dynamics and Beyond, Oxford University Press, Oxford, 2001.
[13] A. J. C. Ladd, Numerical simulations of particulate suspensions via a discretized Boltzmann equation. Part 1. Theoretical foundation, J. Fluid Mech., 271 (1994), 285-309.
[14] A. J. C. Ladd, Hydrodynamic screening in sedimenting suspensions of non-Brownian spheres, Phys. Rev. Lett., 76 (1996), 1392-1395.
[15] A. J. C. Ladd, Sedimentation of homogeneous suspensions of non-Brownian spheres, Phys. Fluids, 9 (1997), 491-499.
[16] Y. Sui, Y. T. Chew, P. Roy, and H. T. Low, A hybrid method to study flow-induced deformation of three-dimensional capsules, J. Comput. Phys., 227 (2008), 6351-6371.
[17] Y. Sui, H. T. Low, Y. T. Chew, and P. Roy, Tank-treading, swinging, and tumbling of liquid-filled elastic capsules in shear flow, Phys. Rev. E, 77 (2008), 016310.
[18] M. M. Dupin, I. Halliday, C. M. Care, L. Alboul, and L. L. Munn, Modeling the flow of dense suspensions of deformable particles in three dimensions, Phys. Rev. E, 75 (2007), 066707.
[19] M. M. Dupin, I. Halliday, C. M. Care, and L. L. Munn, Lattice Boltzmann modelling of blood cell dynamics, Int. J. Comput. Fluid Dyn., 22 (2008), 481-492.
[20] M. Yoshino and T. Murayama, A lattice Boltzmann method for a two-phase flow containing solid bodies with viscoelastic membranes, Eur. Phys. J. Special Topics, 171 (2009), 151-157.
[21] T. Inamuro, Lattice Boltzmann methods for viscous fluid flows and for two-phase fluid flows, Fluid Dyn. Res., 38 (2006), 641-659.
[22] T. Inamuro, R. Tomita, and F. Ogino, Lattice Boltzmann simulations of drop deformation and breakup in shear flows, Int. J. Mod. Phys. B, 17 (2003), 21-26.
[23] T. Inamuro and T. Ii, Lattice Boltzmann simulation of the dispersion of aggregated particles under shear flows, Math. Comput. Simul., 72 (2006), 141-146.
[24] E. Evans and Y. C. Fung, Improved measurements of the erythrocyte geometry, Microvasc. Res., 4 (1972), 335-347.
[25] E. A. Evans, Minimum energy analysis of membrane deformation applied to pipet aspiration and surface adhesion of red blood cells, Biophys. J., 30 (1980), 265-284.
[26] Y. Sone, Asymptotic theory of flow of rarefied gas over a smooth boundary II, In Rarefied Gas Dynamics, ed. D. Dini, Editrice Tecnico Scientifica, Pisa, 2 (1971), 737-749.
[27] T. Inamuro, M. Yoshino, and F. Ogino, Accuracy of the lattice Boltzmann method for small Knudsen number with finite Reynolds number, Phys. Fluids, 9 (1997), 3535-3542.
[28] G. I. Zahalak, P. R. Rao, and S. P. Sutera, Large deformations of a cylindrical liquid-filled membrane by a viscous shear flow, J. Fluid Mech., 179 (1987), 283-305.
[29] K. S. Sheth and C. Pozrikidis, Effects of inertia on the deformation of liquid drops in simple shear flow, Comput. Fluids, 24 (1995), 101-119.
[30] J. Li, Y. Y. Renardy, and M. Renardy, Numerical simulation of breakup of a viscous drop in simple shear flow through a volume-of-fluid method, Phys. Fluids, 12 (2000), 269-282.
[31] J. Beaucourt, F. Rioual, T. Séon, T. Biben, and C. Misbah, Steady to unsteady dynamics of a vesicle in a flow, Phys. Rev. E, 69 (2004), 011906.
[32] V. Vitkova, M. Mader, T. Biben, and T. Podgorski, Tumbling of lipid vesicles, enclosing a

viscous fluid, under a shear flow, J. Optoelectron. Adv. Mater., 7 (2005), 261-264.
[33] P. Gaehtgens and H. Schmid-Schönbein, Mechanisms of dynamic flow adaptation of mammalian erythrocytes, Naturwissenschaften, 69 (1982), 294-296.
[34] R. Waugh and E. A. Evans, Thermoelasticity of red blood cell membrane, Biophys. J., 26 (1979), 115-131.
[35] R. E. Waugh and R. M. Hochmuth, Chapter 60: Mechanics and deformability of hematocytes, In: ed. J. D. Bronzino, Biomedical Engineering Fundamentals, 3rd ed. CRC Press, Boca Raton, 2006.
[36] R. Skalak and S. Chien, Handbook of Bioengineering, McGraw-Hill, New York, 1987.